

Monte Carlo Simulations of Nanoscale Electrical Inhomogeneity in Organic Light-Emitting Diodes and Its Impact on Their Efficiency and Lifetime

Yufei Shen and Noel C. Giebink*

Department of Electrical Engineering, The Pennsylvania State University, University Park, Pennsylvania 16802, USA

(Received 16 July 2015; revised manuscript received 6 October 2015; published 25 November 2015)

The performance of organic light-emitting diodes (OLEDs) has traditionally been understood on the basis of one-dimensional (1D) models that exploit their planar symmetry. Recently, however, full 3D models have predicted that the current density in these devices is in fact laterally inhomogeneous and highly filamentary on the nanoscale. Here, we implement a 3D kinetic Monte Carlo model to understand the factors that underlie electrical inhomogeneity in OLEDs and explore how it affects their quantum efficiency roll-off and operational lifetime. We find that current filaments initiate at both injecting contacts and internal organic-organic layer interfaces, driven by local injection barrier minima and propagated by percolation paths that naturally occur within the disordered molecular-site distribution. In a classic bilayer OLED, electron and hole filaments are observed to coexist in the same layer and can bypass one another, resulting in substantial efficiency loss due to charge imbalance. In the case of a double-heterostructure phosphorescent OLED, inhomogeneity leads to locally enhanced exciton-polaron annihilation rates that account for an approximately threefold reduction in the operating lifetime and an order-of-magnitude decrease in the critical current density for quantum efficiency roll-off. These results underscore the importance of considering the 3D nature of current transport in OLEDs and point to an unexpected role of organic heterojunctions in exacerbating the degree of inhomogeneity in multilayer devices.

DOI: [10.1103/PhysRevApplied.4.054017](https://doi.org/10.1103/PhysRevApplied.4.054017)

I. INTRODUCTION

Organic light-emitting diodes (OLEDs) have advanced dramatically since their inception and are now being commercialized by the display industry [1]. Despite this progress, the intrinsic operational lifetime of OLEDs and their external quantum efficiency (EQE) roll-off at high brightness persist as technical challenges for the field that are particularly important for expansion into the solid-state lighting sector [2–4]. Following significant research addressing both of these issues, neither is yet understood well enough to direct material or device design for systematic improvement; however, it is empirically clear that both phenomena depend strongly on device current density [1,4].

Most understanding to date is built on the assumption that current injection, transport, and recombination in OLEDs can be described by one-dimensional (1D) models that exploit the planar symmetry of these thin-film devices [5–7]. Recently, however, 3D kinetic Monte Carlo (KMC) modeling efforts have predicted that these processes are in fact locally inhomogeneous and highly filamentary on the 10–100-nm length scale due to weak electronic coupling and strong energetic disorder in organic semiconductor thin films [8–14]. This prediction is challenging to explore experimentally, yet it holds significant implications for OLED efficiency and lifetime, since it implies that these

characteristics depend on locally higher current, charge, and exciton densities than previously acknowledged.

Coehoorn and co-workers have recently used a 3D KMC model to explore EQE roll-off and lifetime in a model phosphorescent OLED and understand how these aspects depend on material and device parameters such as heterostructure energy-level alignment, mobility, phosphorescent-dye concentration, and energetics relative to the host [15,16]. While these simulations implicitly account for 3D current and exciton transport, the explicit impact of the associated lateral inhomogeneity on EQE roll-off and lifetime has not been discussed. Given that local current densities are predicted to exceed the spatial average by more than an order of magnitude, this raises the question: How much efficiency and lifetime loss is presently associated with the existence of local hot spots, and how much improvement could be achieved by controlling them?

Here, we implement a 3D KMC model to identify the physical factors that cause electrical inhomogeneity in OLEDs and statistically quantify its impact on EQE roll-off and lifetime in a prototypical double-heterostructure (DH) phosphorescent device. We find that current filamentation originates at the injecting contacts and at internal heterostructure energy barriers, driven by local injection barrier minima and percolation paths that occur naturally within the disordered molecular-site distribution. In a canonical bilayer fluorescent OLED, electron and hole filaments can exist in the same layer and bypass one another, leading to substantial charge imbalance loss.

*ncg2@psu.edu

Extending the model to a DH phosphorescent OLED and incorporating molecular degradation based on triplet exciton-polaron annihilation interactions, we find that current inhomogeneity accounts for more than a threefold reduction in the operating lifetime and an order-of-magnitude decrease in the critical current density for EQE roll-off. These results point to the importance of considering the 3D nature of current and exciton distributions in nominally 1D OLEDs and suggest that avoiding sharp layer interfaces in favor of graded heterojunctions within the device structure may provide a practical route to reduce the degree of current inhomogeneity.

This paper is organized as follows. Section II outlines the 3D KMC model used in this study, and Sec. III A applies it to understand the factors that determine current inhomogeneity in a unipolar single-layer device. The model is extended to a bilayer fluorescent OLED in Sec. III B to understand how current filamentation affects the recombination distribution at an interface and subsequently to a DH phosphorescent device in Sec. III C, where the effects of inhomogeneity on EQE roll-off and lifetime are examined. Section IV discusses the generality of these findings in regard to different model assumptions and considers possible experimental observables that could help assess their validity. Section V concludes with a summary of key results.

II. SIMULATION

We adopt a model similar to that previously described by Mesta *et al.* [9] and Coehoorn *et al.* [15]. Briefly, molecules are assigned to a 3D cubic lattice with site dimensions $N_x \times N_y \times N_z$, where $N_y = N_z = 100$ and current flows in the layer normal (\hat{x}) direction. The lattice constant $a = 1$ nm, and device thicknesses range between 20 and 90 nm (i.e., $20 \leq N_x \leq 90$). The hopping rate for electrons and holes is described via the usual Miller-Abrahams expression [17,18]:

$$W_{ij} = \nu_0 \exp\left\{-2\alpha R_{ij} - \frac{(E_j - E_i)}{k_B T}\right\} \quad (E_j > E_i),$$

$$W_{ij} = \nu_0 \exp\{-2\alpha R_{ij}\} \quad (E_j \leq E_i), \quad (1)$$

where ν_0 is the attempt-to-hop frequency, α is the inverse wave function decay length, k_B is Boltzmann's constant, and R_{ij} is the distance between sites i and j with corresponding site energies E_i and E_j , respectively. Note that ν_0 in this case is the intrinsic attempt-to-hop frequency as opposed to the nearest-neighbor hopping frequency used by some authors [15,16]. All simulations are carried out at room temperature $T = 300$ K. The total energy of an electron or hole on a given site i consists of four parts: (i) the molecular-site energy, (ii) the image potential induced by each electrode, (iii) the Coulomb interaction with other charge carriers and their associated image potentials, and (iv) the potential of the applied electric field. The highest occupied and lowest unoccupied molecular orbital energies associated with each site (E_{HOMO} and E_{LUMO} , respectively) are initialized for each different

OLED material according to a correlated Gaussian disorder model defined via their corresponding standard deviations σ_{HOMO} and σ_{LUMO} , respectively, which are set equal to σ for simplicity [19–21]. In this model, spatial correlations in the site energy arise from random permanent dipole orientations associated with each molecule, which lead to an energy correlation function that decays inversely with the separation distance between sites. Previous authors have established evidence for correlated disorder in common OLED materials [22]; however, it is important to point out that similar degrees of electrical inhomogeneity are found for both correlated and uncorrelated disorder as established in Ref. [14]. The infinite series image potential contribution for each charge between the two perfectly conducting electrodes is given analytically via a digamma function (see the Appendix).

The Coulomb interaction between different charges is more difficult to treat owing to its long-range, nonconverging nature. To reduce the computational expense, we treat the Coulomb interaction of a given charge carrier with all others in the device according to the sum of explicit Coulomb contributions from charges in the immediate vicinity (those within a radius $R \leq \sqrt{3}a$ along with their image charges) together with a mean-field space-charge contribution that approximates the effect of all other, more distant charges in the device [14]. This latter contribution is calculated by determining the layer-averaged charge density along the \hat{x} direction and then solving the 1D Poisson equation subject to the electrode boundary conditions to yield the mean-field electrostatic contribution for a charge in each layer. Contributions (i)–(iv) are summed and updated after each hop to give the initial and final energies used in Eq. (1).

In the event an electron hops onto the site occupied by a hole or vice versa, a singlet or triplet exciton is formed with branching ratio of 1:3 according to spin statistics. Singlet exciton diffusion is dominated via Förster-type hopping with a transfer rate given by [23,24]

$$\Gamma_F = \frac{1}{\tau_S} \left(\frac{R_0}{R_{ij}}\right)^6, \quad (2)$$

where τ_S is the singlet lifetime of molecule i and R_0 is the Förster radius between molecules i and j given by the overlap between their respective emission and absorption spectra. In contrast, triplet diffusion occurs via exchange coupling and is treated as a Dexter process [24,25] with a Miller-Abrahams hopping rate:

$$\Gamma_D = \nu_D \exp\left\{-2\alpha R_{ij} - \frac{(\Delta E_{G,j} - \Delta E_{G,i})}{k_B T}\right\} \quad (\Delta E_{G,j} > \Delta E_{G,i}),$$

$$\Gamma_D = \nu_D \exp\{-2\alpha R_{ij}\} \quad (\Delta E_{G,j} \leq \Delta E_{G,i}), \quad (3)$$

that decreases exponentially with increasing distance from the attempt-to-hop frequency prefactor ν_D . The magnitude of this prefactor is estimated based on a typical triplet diffusion coefficient, $D \sim 10^{-7}$ cm² s⁻¹ [26], according to the relationship $D = (1/6)a^2\Gamma_D$, for a random walker on a

cubic lattice [24], where Γ_D from Eq. (3) is evaluated at the nearest-neighbor separation a . Because the extent to which triplet transfer among spatially separated phosphorescent guest molecules via Förster transfer is still a matter of debate [27,28], we do not include this as a mechanism for triplet diffusion. Although we neglect it here for simplicity, triplet exciton energetic disorder could also be accounted for via the difference in molecular energy gap (i.e., $\Delta E_G = E_{\text{HOMO}} - E_{\text{LUMO}}$) between molecules i and j , assuming a constant exciton binding energy E_B . Table 1 summarizes the key parameter values used in our model.

Annihilation reactions between two excitons (XXA) or between an exciton and a polaron (XPA) are also possible [24,26,29]. Because the physical nature of these interactions varies depending on the involved constituents as well as on various material-specific factors, we treat all annihilation processes as contact interactions for simplicity [16]. For example, an XPA event occurs when an exciton hops onto a neighboring polaron or vice versa. Following XPA, the exciton is removed from the simulation and the polaron remains, whereas the products of XXA depend on the spin states of the reactants. If both excitons are singlets, the final product is one singlet on the target hopping site, whereas singlet annihilation with a triplet leaves only the triplet as a product. When both excitons are triplets, three of the nine pair states have partial singlet character, and so we approximate the singlet formation probability as 1/3 (i.e., the upper limit to the actual probability, which depends on the kinetics of the pair state interaction), with the balance leading to triplet formation [24,30].

Previous investigations seeking to understand the photo-physical processes responsible for intrinsic OLED operational degradation point toward chemical transformation of the emitter and/or host molecules originating from instability of excitons, cations, anions, or annihilation interactions between these species [4,31–34]. Following a number of

recent reports [33,35–37], we focus our study on the effect of exciton-polaron annihilation-induced molecular degradation, though monomolecular exciton and cation-anion degradation modes have also been evaluated for completeness. Since it takes 24 h of CPU time per node to simulate approximately 100 μs of device operation, we accelerate the degradation process by assuming that every annihilation event results in degradation of the target molecule, which subsequently becomes nonemissive and also a charge trap with a singly occupied molecular orbital (SOMO) energy level located in the middle of the host band gap [34,38]. In actuality, the probability of molecular degradation following an XPA event is estimated to be much lower, of the order of 10^{-9} [33]. Aside from the scaling difference in OLED lifetime, however, the assumption of high degradation probability does not change the functional dependence of the simulation results.

Simulations are initiated with an empty device followed by charge-carrier hopping from both electrodes into the bulk. After a given number of KMC steps, the total number of electrons and holes in the device stabilizes and fluctuates around a fixed, steady-state value. The number of KMC steps required to reach this steady-state regime depends strongly on the size of the simulation volume and the energetic disorder widths σ of the involved materials. For a $90 \times 100 \times 100 \text{ nm}^3$ double-heterojunction phosphorescent OLED under moderate driving voltages ($<15 \text{ V}$), it takes approximately 10^8 KMC steps to reach the steady state.

Once the steady state is reached, this configuration is then used to record a “measurement” of current density or emitted light intensity (proportional to the number of exciton recombination events per unit time) over the course of an additional 10^8 KMC steps. If molecular degradation is to be included, steady-state conditions are achieved first, and then the device is allowed to degrade, capturing degraded device configurations at various time intervals. These degraded configurations are subsequently used as the starting point for additional KMC measurements to determine current density, light emission, and other device metrics at each degradation time point.

Simulations are carried out on the National Science Foundation Extreme Science and Engineering Discovery Environment (XSEDE) supercomputing network using a total of 150 Intel Xeon E5-2680 (2.7 GHz) cores. Each core is tasked with single measurements, which typically run for 12–24 h depending on the charge-carrier density inside the device. A total CPU time of approximately 300 000 h is required to complete all of the simulations presented in this study.

III. RESULTS

A. Current inhomogeneity in unipolar devices

We begin by examining a single-layer, hole-only device consisting of a 20-nm-thick layer of N, N' -bis(1-naphthyl)- N, N' -diphenyl-1, 1'-biphenyl-4, 4'-diamine (NPD) sandwiched between indium tin oxide (ITO) and LiF/Al

TABLE 1. Summary of important simulation parameters.

| Parameter | Value | Description |
|--------------|-----------------------------------|--|
| ν_0 | $5 \times 10^{10} \text{ s}^{-1}$ | Attempt-to-hop frequency for charge carriers |
| σ | 0–100 meV | Standard deviation of molecular-site energy distribution |
| a | 1 nm | Lattice constant |
| α | 3.3 nm^{-1} | Inverse wave function decay length |
| ϵ_r | 3 | Relative permittivity |
| E_B | 1 eV | Exciton binding energy |
| $R_{0,HH}$ | 1.2 nm | Förster radius for host-to-host energy transfer |
| $R_{0,HG}$ | 3.5 nm | Förster radius for host-to-guest energy transfer |
| ν_D | $1 \times 10^{11} \text{ s}^{-1}$ | Rate constant prefactor for Dexter transfer |
| τ_G | 1.6 μs | Guest phosphor exciton lifetime |

contacts. Figure 1(a) presents a shaded rendering of the 3D hole current density in the device at an applied bias of 2 V and a disorder strength $\sigma = 75$ meV. Similar to previous observations [8], the current is strongly inhomogeneous, with peak current densities (>10 A/cm²) exceeding the spatial average (0.5 A/cm²) by more than an order of magnitude. In general, filaments tend to originate at the ITO injecting contact, which follows intuitively from the fact that it constitutes an equipotential and therefore enables holes to naturally seek the lowest-energy molecular sites at the interface (i.e., a locally lower injection barrier) [10]. More surprisingly, however, many filaments survive the transition from the interfacial region (loosely defined as the first two monolayers adjacent to the contact) into the bulk and persist all the way to the collecting contact with relatively little diffusive spread or changes in direction.

To quantify the degree of current inhomogeneity in a given plane of the device, we define its mathematical discrepancy D_p according to [39]

$$D_p = \left\{ \int_0^1 du |F(u) - F_0(u)|^p \right\}^{1/p}. \quad (4)$$

Here, the \hat{x} component of the current density distribution in the chosen plane is ordered from lowest to highest to give $J(u)$ in terms of the site number u normalized in the range $u \in [0, 1]$. Scaling $J(u)$ such that $\int J(u) du = 1$ provides the basis for the cumulative distribution function $F(u) = \int_0^u J(u') du'$ that can then be compared with the reference $F_0(u)$ for a perfectly uniform current distribution. For the purposes of this study, the infinite order discrepancy ($p = \infty$) provides the most useful and intuitive measure of inhomogeneity, with a definition that simplifies to

$$D = \max_{u \in [0,1]} |F(u) - F_0(u)|. \quad (5)$$

In this case, $D = 0$ corresponds to a uniform current distribution, whereas $D = 1$ for the extreme case in which all current passes through one molecule in the plane. In general, the closer D is to unity, the more laterally inhomogeneous the current distribution is.

Figures 1(b) and 1(c) show how D varies throughout the thickness of the NPD film for different applied biases and energetic disorder strengths. From these data, it is clear that current inhomogeneity depends strongly on the level of disorder in the film and that it tends to be highest near the injecting contact. As shown in Fig. 1(b), increasing the bias has little effect on D in the two-monolayer injection region but does cause it to decay more rapidly into the bulk, indicating that filaments disperse more easily at a higher applied electric field. Though not plotted here, varying the mean hole injection barrier Δ in the range 0–0.8 eV leads to a small increase in the layer-averaged discrepancy from $D = 0.55$ to $D = 0.63$. By contrast, Fig. 1(c) shows that D depends strongly on σ in the range 0–100 meV that is relevant for organic semiconductor thin films [22]. These

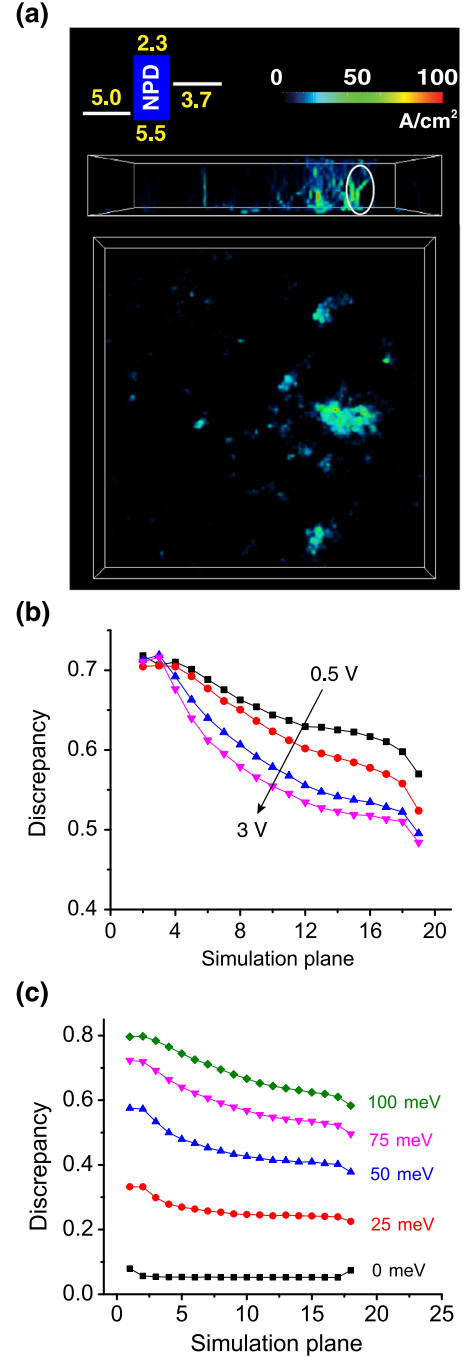


FIG. 1. (a) Three-dimensional visualization of the local current density for a 20-nm-thick NPD hole-only device (energy-level diagram shown in the top left inset) with $\sigma = 75$ meV driven at 2-V bias. The average discrepancy in this case is $D = 0.60$. (b) Discrepancy evaluated in each simulation plane of the NPD film for different applied biases $V_0 = 0.5, 1, 2,$ and 3 V; the corresponding average device current densities are 20, 96, 554, and 1392 mA/cm², respectively. In these simulations, the disorder strength is $\sigma = 75$ meV, and the anode injection barrier is $\Delta = 0.5$ eV. (c) Change in discrepancy for σ varying in 25-meV increments as indicated by the labels ($V_0 = 2$ V, $\Delta = 0.5$ eV). In order, the associated current densities are 389, 449, 573, 554, and 400 mA/cm².

observations are consistent with those reported by van der Holst *et al.* [8] and indicate that varying the bias and injection barrier can influence the degree of current inhomogeneity, but on-site energetic disorder is the underlying and dominant factor. We also examine the case of uncorrelated Gaussian disorder and find the results to be functionally similar to those in Fig. 1(c), but with a discrepancy typically about 30% lower, confirming that current inhomogeneity is significant irrespective of site energy correlations as established previously [14].

Figure 2(a) examines the origin of filaments in more detail for a $\sigma = 75$ meV device by overlaying white contour lines encircling local current densities $J > 9$ A/cm² (for reference, the area-average current density

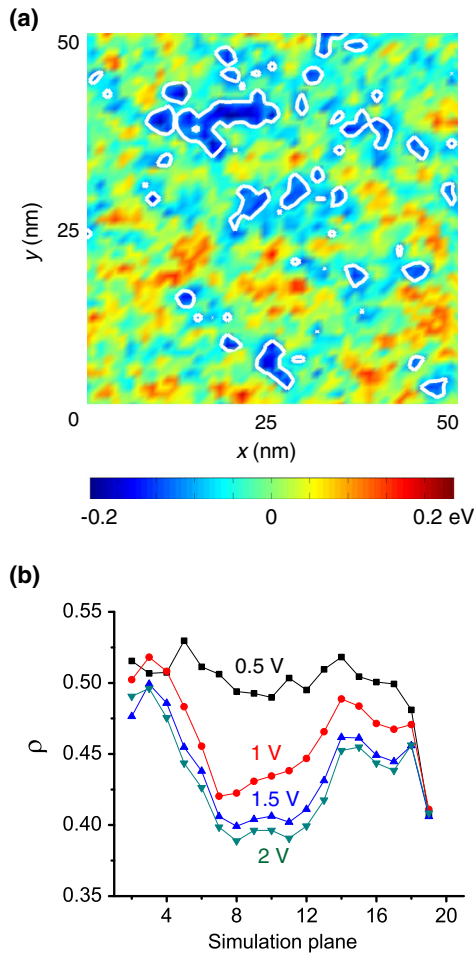


FIG. 2. (a) False-color map of the on-site energy distribution in the monolayer of NPD molecules adjacent to the injecting ITO anode. White contour lines superimposed on this plot indicate local current densities >9 A/cm². (b) Correlation coefficient between on-site energy and local current density in each simulation plane of the device for varying applied biases. The decrease in ρ with an increasing bias indicates that charge carriers begin hopping to previously unfavorable, higher-energy sites due to the added electrostatic potential, which is responsible for the discrepancy trend observed in Fig. 1(b).

$J_{\text{avg}} = 0.1$ A/cm² and $D = 0.71$) on top of a false-color map of the on-site energies (relative to the mean HOMO energy) in the first monolayer adjacent to the injecting ITO contact. The clear correlation between regions with high current and low site energy (dark blue) confirms the intuitive expectation mentioned above that filaments initiate from local injection barrier minima.

This relationship can be quantified by calculating the Pearson linear correlation coefficient:

$$\rho = \frac{\langle J(y, z)E(y, z) \rangle - \langle J(y, z) \rangle \langle E(y, z) \rangle}{\sqrt{\langle J^2(y, z) \rangle - \langle J(y, z) \rangle^2} \sqrt{\langle E^2(y, z) \rangle - \langle E(y, z) \rangle^2}}, \quad (6)$$

which is the covariance of local current density (J) and site energy (E) distributions in a given plane normalized by their respective standard deviations. Although not a perfect measure of the correlation between J and E owing to their generally nonlinear relationship, Eq. (6) nevertheless provides a reasonable starting point to evaluate the association between these quantities. Figure 2(b) plots ρ for each layer of the device at different biases ranging from 0.5 to 2 V, demonstrating that regions of high local current maintain a strong correlation with low-energy sites deep into the bulk. In other words, once initiated, filaments evolve in a percolating fashion through the bulk by following regions of lower site energy, which can lead to lateral “kinks” as circled in Fig. 1(a). Correlation in the bulk decreases with increasing bias, because the applied field increasingly favors forward hops to (previously inaccessible) higher-energy sites, thereby providing a mechanism for filaments to disperse.

Given the important role of injection in initiating filaments observed above, it is natural to explore what happens at an internal organic heterojunction barrier; namely, how does a filamentary current distribution evolve through an interface? Figure 3 addresses this question by simulating a hole-only ITO/20 nm NPD/70 nm tris(4-carbazoyl-9-ylphenyl)amine (TCTA)/LiF/Al device featuring a mean NPD-to-TCTA HOMO barrier $\Delta = 0.2$ eV. From the visualization in Fig. 3(a), it is apparent that some NPD filaments persist through the barrier, whereas, in other cases, the barrier initiates *new* filaments in TCTA (solid oval). This latter observation is perhaps surprising, since it is not obvious where the holes that feed these new filaments are supplied from. Closer inspection reveals that lateral diffusion can be significant for the large (inhomogeneous) hole density accumulated at the interface, to the extent that it provides a pathway for holes to seek out regions of the interface with a locally lower injection barrier and subsequently initiate new filaments in much the same manner as from a contact. The result of this behavior is that the interface enhances inhomogeneity, as evidenced in Fig. 3(b) by peaks in D that occur at the NPD-TCTA interface.

When the disorder strength is the same for both materials (solid black squares), the interface peak in D recovers

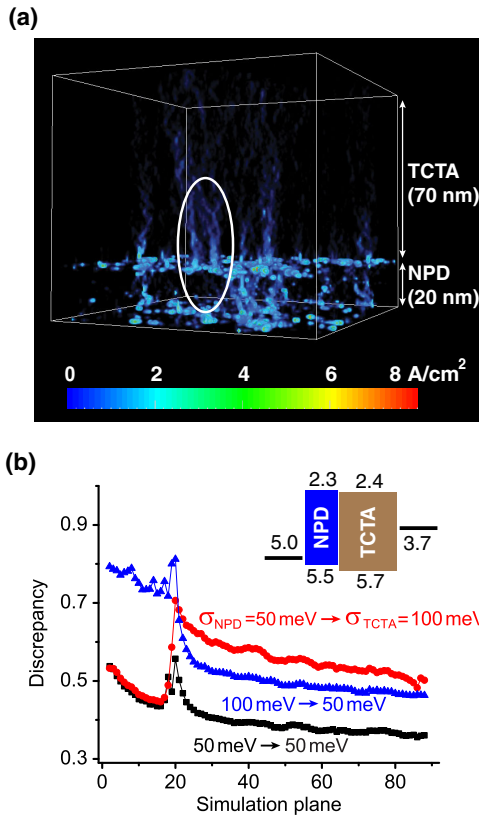


FIG. 3. (a) Visualization of the local current density in a hole-only heterojunction device consisting of ITO/NPD/TCTA/LiF/Al operated at an applied bias of 7 V; the inset in (b) shows the device energy-level diagram. The solid oval highlights new current filaments that emerge at the NPD-TCTA interface. (b) Discrepancy calculated for each simulation plane of different NPD and TCTA devices in which the disorder strength on either side of the heterojunction is varied. All simulations are carried out at a constant 7-V bias (with associated current densities in the range 52–75 mA/cm²), and the mean NPD to TCTA hole injection barrier is maintained at $\Delta = 0.2$ eV.

within a few monolayers back to the bulk-determined value expected for a single-layer device. Current transitioning the same interface barrier ($\Delta = 0.2$ eV) from a less disordered NPD layer into more disordered TCTA (solid red circles) displays increased inhomogeneity in the bulk of the latter as intuitively expected. Interestingly, however, the opposite transition from more disordered NPD to less disordered TCTA (solid blue triangles) leads to a bulk discrepancy in the latter that is higher than that for a single layer of the same TCTA. Evidently, the disorder strength of one organic layer can influence the current inhomogeneity in the next layer, presumably because strong filaments initiated in one layer can persist into the next.

B. Inhomogeneity in bipolar heterojunction OLEDs

Proceeding from unipolar to bipolar devices, Fig. 4(a) visualizes the simulation of a classic NPD (40 nm, $\sigma = 75$ meV)/tris(8-hydroxyquinolino)aluminum (Alq₃,

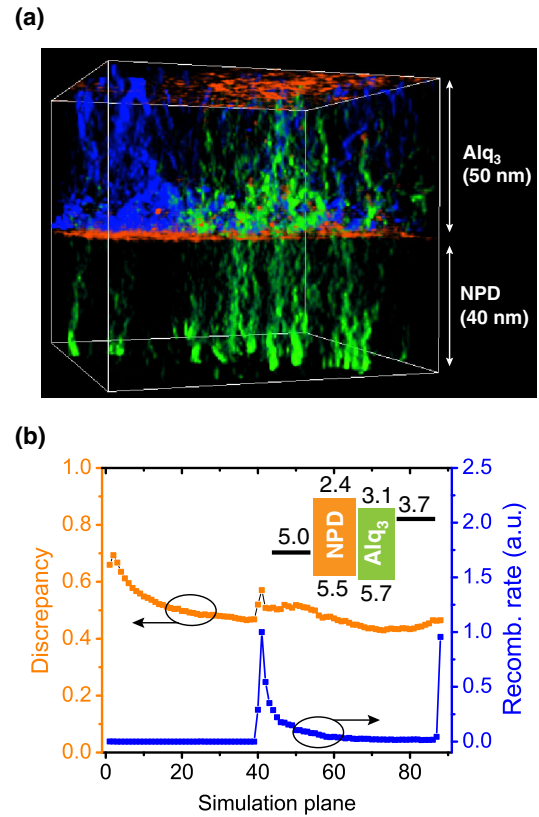


FIG. 4. (a) Visualization of the local electron (blue) and hole (green) current densities together with the resulting recombination-rate distribution (red) in a bilayer ITO/NPD/Alq₃/LiF/Al OLED operating at 7-V applied bias with an average current density $J_{\text{avg}} = 400$ mA/cm². The disorder strength for both NPD and Alq₃ is set equal at $\sigma = 75$ meV. (b) Total current discrepancy (orange) and normalized recombination rate (blue) in each simulation plane of the device. The NPD/Alq₃ interface is located at simulation plane 40/41.

50 nm, $\sigma = 75$ meV) bilayer OLED operating at 7-V applied bias and an average current density $J_{\text{avg}} = 400$ mA/cm². There, both hole (green) and electron (blue) filaments are evident, and together they lead to the local recombination-rate distribution shown in red. While the majority of recombination occurs in Alq₃ near the heterojunction interface as expected [cf. Fig. 4(b)] [5], it is also clear that hole leakage filaments can initiate into Alq₃ and “miss” the existing electron filaments, resulting in substantial surface recombination loss at the cathode. In fact, electron and hole filaments might nominally be expected to avoid one another in the same material, since, for a fixed HOMO-LUMO gap, on-site hole and electron energies trend oppositely, and therefore the same set of molecular sites cannot serve as energy minima for both carrier types. Whether this is truly the case, however, remains an open question, since excitonic energy disorder implies some degree of variation in the transport gap which might result in uncorrelated, or even negatively correlated, HOMO and LUMO levels that are more favorable for recombination.

Figure 4(b) shows that the coexistence of hole and electron filaments in the same layer increases the total current discrepancy in the Alq₃ recombination zone, causing more than half of the recombination events in this region to occur on <2% of the available molecules.

Figure 5(a) examines the internal quantum efficiency (IQE) of devices with varying disorder (equal for both layers) as a function of average current density. The strong IQE decrease with increasing disorder observed at low to moderate current densities ($J_{\text{avg}} < 100 \text{ mA/cm}^2$) is directly associated with growing inhomogeneity according to Fig. 5(b). At low current with no disorder, electrons and holes recombine quantitatively, and the IQE approaches the fluorescent OLED limit of 0.25 (unity photoluminescent quantum yield is assumed) [40]. As disorder and filamentation increase, hole leakage in the manner of Fig. 4(a) increases, leading to greater charge imbalance loss. This effect is less pronounced at high bias (blue triangles),

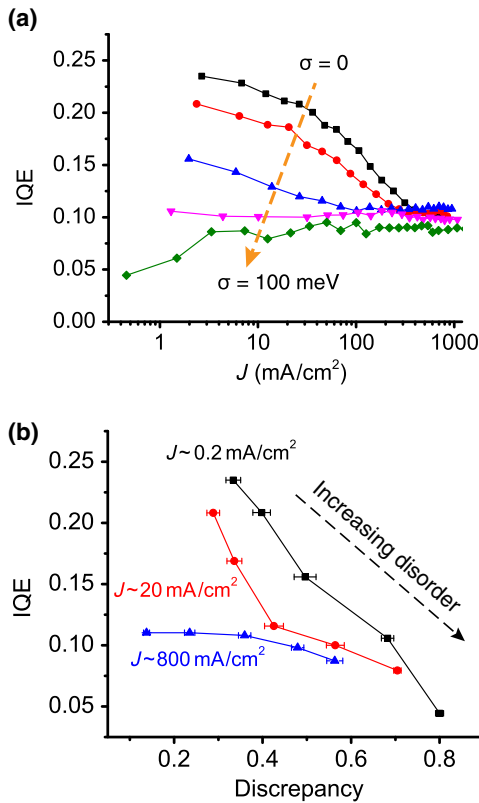


FIG. 5. (a) IQE versus current density for NPD/Alq₃ devices with disorder strengths σ ranging 0 to 100 meV in 25-meV increments. (b) IQE at three different constant current densities versus the average current discrepancy for the devices in (a); error bars reflect the variation in discrepancy within the device. At lower current densities, the IQE trends inversely with the discrepancy due to spatial mismatch between electron and hole filaments that bypass one another in the Alq₃ layer. This dependence is weaker at high bias because the IQE loss in all devices is dominated by the reduced recombination probability owing to faster hole transit through the Alq₃ layer.

$J_{\text{avg}} \sim 800 \text{ mA/cm}^2$), since the stronger applied field reduces the degree of inhomogeneity; cf. Fig. 1(b). At high applied bias, charge imbalance limits the efficiency of all the devices irrespective of their disorder because the reduced recombination probability resulting from faster hole transit through Alq₃ outweighs any effects of electron and hole filaments spatial mismatch.

C. Impact on efficiency roll-off and lifetime in phosphorescent OLEDs

Figure 6 simulates a prototypical DH phosphorescent OLED consisting of a 40-nm-thick NPD hole transport layer, a 10-nm-thick 4, 4'-bis(*N*-carbazolyl)-1, 1'-biphenyl (CBP) emissive layer (EML) doped with 10 wt % of the green phosphorescent dye tris[2-phenylpyridinato-C₂,N] iridium(III) [Ir(ppy)₃], and a 40-nm-thick bathocuprouine (BCP) electron transport layer [41]. As shown in Fig. 6(a) and established experimentally, the double heterostructure more effectively confines electrons and holes within the emissive layer, eliminating charge imbalance (i.e., current leakage from the EML) and enabling unity IQE for all

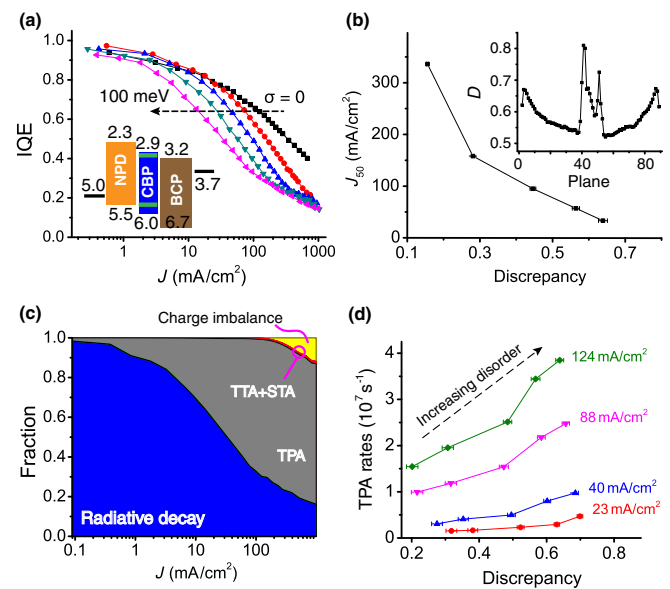


FIG. 6. (a) IQE versus current density for phosphorescent devices with varying disorder strengths. The inset diagram shows the energy-level structure of the simulated OLED; the disorder strength is equal in all layers of the device. (b) Critical current density for IQE roll-off, J_{50} , as a function of the current discrepancy in the emissive layer. The inset shows the discrepancy profile for the entire device with $\sigma = 75 \text{ meV}$. (c) Relative contribution of different quantum efficiency loss pathways as a function of device current density. TPA is the dominant loss at operationally relevant currents. (d) Average TPA rate at several constant (average) current densities plotted versus the current discrepancy in devices with varying disorder strengths. Increased current inhomogeneity leads to increased TPA that is responsible for the faster roll-off shown in (a). Error bars in (b) and (d) reflect the variation in discrepancy within the emissive layer.

disorder strengths at low current. In this case, however, increasing the disorder strength causes the IQE to roll-off at increasingly lower current densities, with the transition from $\sigma = 0$ to $\sigma = 100$ meV resulting in an order-of-magnitude decrease in the critical current density J_{50} , at which the IQE reaches half its maximum value. Plotting J_{50} versus the EML-averaged current discrepancy in Fig. 6(b) clearly points to inhomogeneity as a significant factor underlying the stronger IQE roll-off. Indeed, the inset plot shows that D increases significantly within the EML, presumably due to the interface effect identified in Fig. 4(b) except more so in this case, since there are two closely spaced energy barrier interfaces for carrier accumulation and filament initiation.

The link between inhomogeneity and roll-off is understood to result from triplet-polaron annihilation (TPA) [29,42], which is the primary IQE loss pathway for this device as shown in Fig. 6(c). The dominant role of TPA loss observed here is consistent with the results of van Eersel *et al.* [16] and stems from the combination of relatively long triplet and polaron lifetimes. From a qualitative standpoint, current and recombination inhomogeneity would be expected to exacerbate TPA loss owing to the locally increased triplet and polaron densities associated with recombining filaments. Figure 6(d) shows that this is indeed the case borne out in simulation, where the average TPA rate in the EML increases approximately linearly with its current discrepancy.

In addition to efficiency loss, the increase in the TPA rate due to filamentation also has the potential to reduce the OLED operational lifetime, since exciton-polaron annihilation reactions are an established pathway for molecular degradation in the EML of phosphorescent OLEDs [33,35–37]. Figure 7(a) simulates the normalized luminance versus time degradation characteristic for the same phosphorescent OLED structure under varying current drives based on the accelerated TPA degradation assumptions outlined in Sec. II. The results are qualitatively consistent with the functional form and current density dependence observed experimentally in a variety of phosphorescent OLEDs [33,43]. Error bars associated with each stated current density are due to the fact that J_{avg} is not an independent simulation variable; it is adjusted by changing the applied bias over the course of several trial runs to be within 5% accuracy of its target value.

Figure 7(b) subsequently compares the degradation characteristic for OLEDs with varying disorder strengths at a fixed average current density $J_{\text{avg}} = 40 \pm 1$ mA/cm². It is clear from these results that degradation accelerates with increasing disorder. Quantifying the OLED lifetime LT_{80} as the time to reach 80% of initial luminance [43], Fig. 7(c) demonstrates that this trend is directly linked to the current discrepancy in the EML. There, LT_{80} can vary by a factor of 3 or more depending on how inhomogeneous the current is, with a trend that mirrors the changing TPA

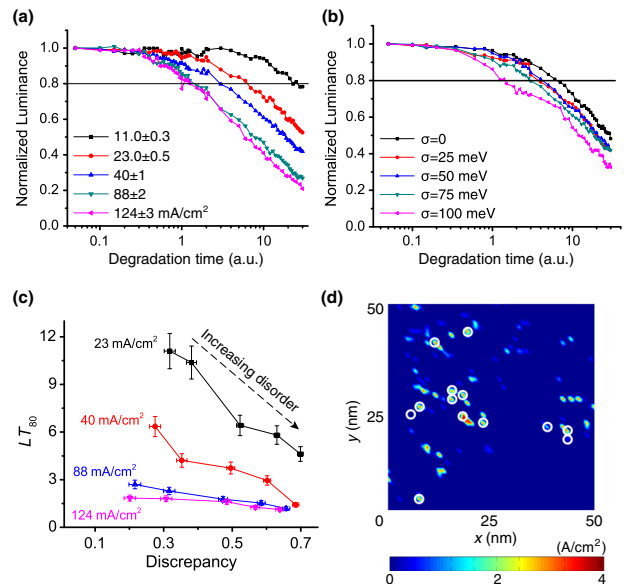


FIG. 7. (a) Normalized luminance versus time for a phosphorescent OLED operated under different constant current densities. The device architecture is the same as in Fig. 6(a), and the disorder strength of all layers is $\sigma = 75$ meV. (b) Normalized luminance versus time degradation characteristic for devices with varying disorder strengths operated at constant current density $J_{\text{avg}} = 40$ mA/cm². (c) Summary of the change in device lifetime LT_{80} with the average current discrepancy in the emissive layer for several constant operating current densities. (d) Positions of degraded molecules (white circles) in a typical simulation plane within the EML overlaid on top of a false-color map of the local current density distribution. This image is acquired from a device with $\sigma = 75$ meV degraded to 20% of initial luminance at a current drive $J_{\text{avg}} = 124$ mA/cm².

rate in Fig. 6(d). Figure 7(d) further emphasizes the link between degradation and current inhomogeneity by overlaying the locations of degraded molecules with the current density distribution in a particular simulation plane within the EML. In general, degraded molecules coincide with current hot spots, resulting in a correlation coefficient $\rho = 0.35$ averaged over all planes in the EML.

Since current inhomogeneity effectively leads to a smaller device active area defined by higher local current densities, it is useful to explore whether the associated IQE and lifetime losses identified above can be described in terms of an increased effective current density, J_{eff} . In the simplified situation of an OLED in which a constant local current density flows through a given subarea, with zero current elsewhere, the average and local effective current densities are related via the discrepancy according to $J_{\text{eff}} = J_{\text{avg}}/(1 - D)$. Despite its crude nature, Fig. 8(a) shows that adopting this approximation largely collapses the variation in IQE roll-off observed for different disorder strengths in Fig. 6(a). Similarly, Fig. 8(b) shows that the previously scattered LT_{80} lifetimes obtained for different disorder strengths as a function of average current density

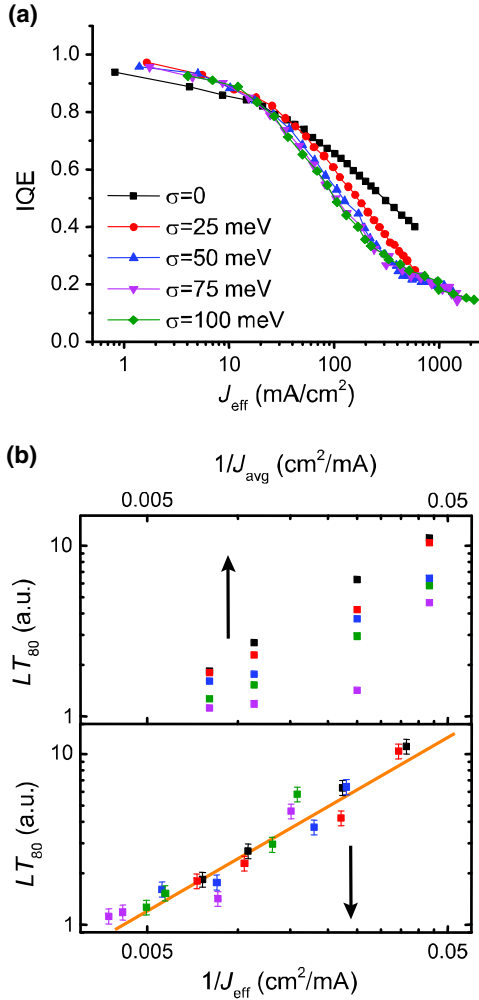


FIG. 8. (a) Plotting the IQE data from Fig. 6(a) in terms of the effective current density $J_{\text{eff}} = J_{\text{avg}}/(1 - D)$ collapses the data for different disorder strengths to a single curve. Deviation in the case of zero disorder strength reflects a breakdown in the applicability of this expression for J_{eff} when the fluctuations in local current density become small. (b) Comparison of device lifetimes plotted versus the inverse of the average current density (upper panel) and the effective current density (lower panel). The linear fit in the lower panel demonstrates that all of the data can be described in terms of the effective current density by a single power-law dependence, $LT_{80} \propto (1/J_{\text{eff}})^\alpha$, with $\alpha = 1.03 \pm 0.06$.

(upper panel) can be consistently described by a single inverse power law in terms of J_{eff} via $LT_{80} \propto (1/J_{\text{eff}})^\alpha$ with $\alpha = 1.03 \pm 0.06$ (lower panel) [43].

IV. DISCUSSION

The IQE and lifetime losses associated with current inhomogeneity in the phosphorescent OLEDs above both stem from exciton-polaron annihilation. Because we model TPA as a contact interaction, whereas longer-range dipole-dipole coupling can mediate TPA between efficient phosphorescent emitters and nearby host polarons, these losses

likely represent a lower bound. More generally, however, any current density-dependent degradation or efficiency loss mechanisms will be exacerbated by inhomogeneity. For example, we find similar lifetime reductions for alternate degradation scenarios based on exciton-exciton annihilation or simple polaron-related (i.e., cationic or anionic) molecular instabilities [31]. A weaker impact is observed for monomolecular exciton-driven degradation (i.e., originating from instability of EML molecular excited states [34,44]), presumably because exciton diffusion tends to counteract inhomogeneity and degrade the device more uniformly. In this case, incorporating excitonic site energy disorder into the model [e.g., via Eq. (3)] could become important, since exciton diffusion would directly influence the location of degraded molecules, in contrast to the TPA mechanism focused on here, where high polaron densities annihilate triplets before they have time to appreciably diffuse.

At this stage, it is important to point out that no direct experimental observations of intrinsic nanoscale current inhomogeneity have been reported for OLEDs to date. The challenge arises because one must noninvasively observe the nanoscale current variation that occurs naturally in an operating device. For example, direct electroluminescence imaging is nontrivial because inhomogeneity occurs on a subdiffraction length scale, whereas scanning probe techniques are complicated by the fact that local current (and their associated potential) variations are buried beneath an injecting contact. Low-frequency $1/f$ current noise spectra of single-layer OLEDs and unipolar devices do indirectly hint toward filamentation and percolative transport, though the small number of such studies presently renders this line of evidence inconclusive [45–47]. Despite the clear need for better experimental characterization, theoretical support remains strong, with current inhomogeneity predicted by numerous Monte Carlo and master equation models for both correlated and uncorrelated disorder in a range of single- and multilayer devices [8–14].

In the context of device observables, electrical inhomogeneity might be inferred from increased EQE roll-off with decreasing temperature in phosphorescent OLEDs dominated by TPA loss. This is because it is ultimately the disorder strength relative to the temperature (the so-called disorder parameter $\hat{\sigma} = \sigma/k_b T$) that affects the nature of transport [8], and thus the effect of halving the temperature is tantamount to doubling the disorder strength in Fig. 6(a). Provided that the luminescence quantum yield and charge balance are not compromised in the process (our model suggests the latter is not), quantifying the temperature dependence of, e.g., J_{50} and interpreting it within the context of Monte Carlo simulations might provide a means to infer the EML discrepancy in real devices.

Beyond the experimental challenge of establishing and understanding current inhomogeneity, there is also the question of identifying what practical steps can be taken to reduce it in state-of-the-art OLEDs. Short of attempting to

engineer host and transport layer materials with less energetic disorder than the $\sigma \sim 100$ meV typical for molecules such as NPD [36], one general conclusion of this work is that sharp internal organic heterojunction barriers should be avoided to minimize their associated spikes in inhomogeneity [e.g., see the discrepancy in the inset in Fig. 6(b)]. Because multilayer phosphorescent OLEDs typically possess many such barriers in close proximity, the level of inhomogeneity in critical regions such as the emissive layer may be worse than it otherwise could be through proper design of these interfaces. Grading layer transitions or even host materials throughout an entire device is one route to accomplish this and has been experimentally found to increase OLED lifetime and reduce annihilation-related EQE roll-off [35,48–51]. Though we do not speculate on how much of this improvement might result from reduced current inhomogeneity, it seems likely that this effect is at least partially responsible as a common thread linking the many different materials and device architectures for which this strategy has been successful.

V. CONCLUSION

In summary, we have carried out kinetic Monte Carlo simulations to understand the origins of nanoscale current inhomogeneity in organic thin films and have characterized its impact on the efficiency and lifetime of phosphorescent OLEDs. We find that filaments tend to originate from injection at contacts and also at internal organic-organic layer interfaces due to disorder-induced variations in the local injection barrier. The discrepancy is introduced as a statistical measure of current inhomogeneity and applied to understand its dependence on the bias, disorder strength, and injection barrier. Electron and hole filaments are observed to coexist in a classic NPD/Alq₃ OLED, bypassing one another in some instances that lead to significant charge imbalance efficiency loss at low and moderate current densities.

In phosphorescent OLEDs subject to triplet-polaron annihilation-induced degradation and efficiency loss, current inhomogeneity peaking in the emissive layer leads to a local effective current density 3 times higher than the spatial average and a corresponding threefold reduction in operating lifetime as well as an order-of-magnitude decrease in the critical current density for EQE roll-off. More broadly, any current density-related aspect of OLED performance is likely to be affected by the inhomogeneity studied here, which should therefore serve as motivation to better understand, characterize, and ultimately control this phenomenon.

ACKNOWLEDGMENTS

We acknowledge S. Mubin and Z. Xu for helpful discussions. High-performance computing resources and services are provided by the Research Computing and Cyberinfrastructure unit of Information Technology Services at the Pennsylvania State University and the

XSEDE, which is supported by National Science Foundation Grant No. ACI-1053575.

APPENDIX: IMAGE INTERACTION OF CHARGE CARRIERS BETWEEN PARALLEL ELECTRODES

In our model, electrons and holes are treated as point charges, and the two electrodes are treated as perfect conductors. As previously discussed by Simmons [52], a charge carrier in the bulk will interact with an infinite series of image charges induced in the surrounding electrodes, which leads to a correction relative to the standard Schottky barrier lowering calculation for one electrode. The image charge interaction lowers the on-site energy of charge carriers according to

$$\begin{aligned} \Delta E_{\text{imag}} &= -\frac{e^2}{8\pi\epsilon} \left\{ \frac{1}{2x} + \sum_{n=1}^{\infty} \left[\frac{nL_x}{(nL_x)^2 - x^2} - \frac{1}{nL_x} \right] \right\} \\ &= -\frac{e^2}{8\pi\epsilon} \left\{ \frac{1}{2x} - \frac{1}{2L_x} \left[\psi^{(0)} \left(1 - \frac{x}{L_x} \right) \right. \right. \\ &\quad \left. \left. + \psi^{(0)} \left(1 + \frac{x}{L_x} \right) + 2\gamma \right] \right\}, \end{aligned}$$

where x is the distance from the anode, L_x is the total device thickness, ϵ is the absolute permittivity, ψ^0 is the digamma function, and $\gamma = 0.577216$ is Euler's constant. This expression typically deviates little from the single-electrode image charge interaction (<1%) at normal device thicknesses; however, it is straightforward to include and requires no added computational cost.

-
- [1] A. Buckley, *Organic Light-Emitting Diodes (OLEDs): Materials, Devices and Applications* (Woodhead, New York, 2013).
 - [2] S. Reineke, M. Thomschke, B. Luessem, and K. Leo, White organic light-emitting diodes: Status and perspective, *Rev. Mod. Phys.* **85**, 1245 (2013).
 - [3] C. Murawski, K. Leo, and M. C. Gather, Efficiency roll-off in organic light emitting diodes, *Adv. Mater.* **25**, 6801 (2013).
 - [4] F. So and D. Kondakov, Degradation mechanisms in small-molecule and polymer organic light-emitting diodes, *Adv. Mater.* **22**, 3762 (2010).
 - [5] B. Ruhstaller, S. A. Carter, S. Barth, H. Riel, W. Riess, and J. C. Scott, Transient and steady-state behavior of space charges in multilayer organic light-emitting diodes, *J. Appl. Phys.* **89**, 4575 (2001).
 - [6] E. Tutis, M. N. Bussac, B. Masenelli, M. Carrard, and L. Zuppiroli, Numerical model for organic light-emitting diodes, *J. Appl. Phys.* **89**, 430 (2001).
 - [7] B. Ruhstaller, T. Beierlein, H. Riel, S. Karg, J. C. Scott, and W. Riess, Simulating electronic and optical processes in multilayer organic light-emitting devices, *IEEE J. Quantum Electron.* **9**, 723 (2003).

- [8] J. J. M. van der Holst, M. A. Uijtewaal, R. Balasubramanian, R. Coehoorn, P. A. Bobbert, G. A. de Wijs, and R. A. de Groot, Modeling and analysis of the three-dimensional current density in sandwich-type single-carrier devices of disordered organic semiconductors, *Phys. Rev. B* **79**, 085203 (2009).
- [9] M. Mesta, M. Carvelli, R. J. de Vries, H. van Eersel, J. J. M. van der Holst, M. Schober, M. Furno, B. Luessem, K. Leo, P. Loeb, R. Coehoorn, and P. A. Bobbert, Molecular-scale simulation of electroluminescence in a multilayer white organic light-emitting diode, *Nat. Mater.* **12**, 652 (2013).
- [10] E. Tutis, I. Batistic, and D. Berner, Injection and strong current channeling in organic disordered media, *Phys. Rev. B* **70**, 161202 (2004).
- [11] N. Rappaport, Y. Preezant, and N. Tessler, Spatially dispersive transport: A mesoscopic phenomenon in disordered organic semiconductors, *Phys. Rev. B* **76**, 235323 (2007).
- [12] J. J. Kwiatkowski, J. Nelson, H. Li, J. L. Bredas, W. Wenzel, and C. Lennartz, Simulating charge transport in tris(8-hydroxyquinoline) aluminium (Alq₃), *Phys. Chem. Chem. Phys.* **10**, 1852 (2008).
- [13] P. Kordt, J. J. M. van der Holst, M. Al Helwi, W. Kowalsky, F. May, A. Badinski, C. Lennartz, and D. Andrienko, Modeling of organic light emitting diodes: From molecular to device properties, *Adv. Funct. Mater.* **25**, 1955 (2015).
- [14] J. J. M. van der Holst, F. W. A. van Oost, R. Coehoorn, and P. A. Bobbert, Monte Carlo study of charge transport in organic sandwich-type single-carrier devices: Effects of Coulomb interactions, *Phys. Rev. B* **83**, 085206 (2011).
- [15] R. Coehoorn, H. van Eersel, P. A. Bobbert, and R. A. J. Janssen, Kinetic Monte Carlo study of the sensitivity of OLED efficiency and lifetime to materials parameters, *Adv. Funct. Mater.* **25**, 2024 (2015).
- [16] H. van Eersel, P. A. Bobbert, R. A. J. Janssen, and R. Coehoorn, Monte Carlo study of efficiency roll-off of phosphorescent organic light-emitting diodes: Evidence for dominant role of triplet-polaron quenching, *Appl. Phys. Lett.* **105**, 143303 (2014).
- [17] A. Miller and E. Abrahams, Impurity conduction at low concentrations, *Phys. Rev.* **120**, 745 (1960).
- [18] H. Bassler, Charge transport in disordered organic photoconductors—A Monte-Carlo simulation study, *Phys. Status Solidi B* **175**, 15 (1993).
- [19] Y. N. Gartstein and E. M. Conwell, High-field hopping mobility in molecular-system with spatially correlated energetic disorder, *Chem. Phys. Lett.* **245**, 351 (1995).
- [20] D. H. Dunlap, P. E. Parris, and V. M. Kenkre, Charge-Dipole Model for the Universal Field Dependence of Mobilities in Molecularly Doped Polymers, *Phys. Rev. Lett.* **77**, 542 (1996).
- [21] S. V. Novikov, D. H. Dunlap, V. M. Kenkre, P. E. Parris, and A. V. Vannikov, Essential Role of Correlations in Governing Charge Transport in Disordered Organic Materials, *Phys. Rev. Lett.* **81**, 4472 (1998).
- [22] S. L. M. van Mensfoort, V. Shabro, R. J. de Vries, R. A. J. Janssen, and R. Coehoorn, Hole transport in the organic small molecule material alpha-NPD: Evidence for the presence of correlated disorder, *J. Appl. Phys.* **107**, 113710 (2010).
- [23] T. Forster, 10th Spiers memorial lecture—Transfer mechanisms of electronic excitation, *Discuss. Faraday Soc.* **27**, 7 (1959).
- [24] M. Pope and C. Swenberg, *Electronic Processes in Organic Crystals and Polymers* (Oxford University Press, New York, 1999).
- [25] D. L. Dexter, A theory of sensitized luminescence in solids, *J. Chem. Phys.* **21**, 836 (1953).
- [26] M. A. Baldo and S. R. Forrest, Transient analysis of organic electrophosphorescence: I. Transient analysis of triplet energy transfer, *Phys. Rev. B* **62**, 10958 (2000).
- [27] Y. Zhang and S. R. Forrest, Triplet diffusion leads to triplet-triplet annihilation in organic phosphorescent emitters, *Chem. Phys. Lett.* **590**, 106 (2013).
- [28] W. Staroske, M. Pfeiffer, K. Leo, and M. Hoffmann, Single-Step Triplet-Triplet Annihilation: An Intrinsic Limit for the High Brightness Efficiency of Phosphorescent Organic Light Emitting Diodes, *Phys. Rev. Lett.* **98**, 197402 (2007).
- [29] S. Reineke, K. Walzer, and K. Leo, Triplet-exciton quenching in organic phosphorescent light-emitting diodes with Ir-based emitters, *Phys. Rev. B* **75**, 125328 (2007).
- [30] R. E. Merrifield, Theory of magnetic field effects on mutual annihilation of triplet excitons, *J. Chem. Phys.* **48**, 4318 (1968).
- [31] H. Aziz, Z. D. Popovic, N. X. Hu, A. M. Hor, and G. Xu, Degradation mechanism of small molecule-based organic light-emitting devices, *Science* **283**, 1900 (1999).
- [32] S. Schmidbauer, A. Hohenleutner, and B. Koenig, Chemical degradation in organic light-emitting devices: Mechanisms and implications for the design of new materials, *Adv. Mater.* **25**, 2114 (2013).
- [33] N. C. Giebink, B. W. D'Andrade, M. S. Weaver, P. B. Mackenzie, J. J. Brown, M. E. Thompson, and S. R. Forrest, Intrinsic luminance loss in phosphorescent small-molecule organic light emitting devices due to bimolecular annihilation reactions, *J. Appl. Phys.* **103**, 044509 (2008).
- [34] D. Y. Kondakov, W. C. Lenhart, and W. F. Nichols, Operational degradation of organic light-emitting diodes: Mechanism and identification of chemical products, *J. Appl. Phys.* **101**, 024512 (2007).
- [35] Y. Zhang, J. Lee, and S. R. Forrest, Tenfold increase in the lifetime of blue phosphorescent organic light-emitting diodes, *Nat. Commun.* **5**, 5008 (2014).
- [36] Q. Wang, B. Sun, and H. Aziz, Exciton-polaron-induced aggregation of wide-bandgap materials and its implication on the electroluminescence stability of phosphorescent organic light-emitting devices, *Adv. Funct. Mater.* **24**, 2975 (2014).
- [37] N. C. Giebink, B. W. D'Andrade, M. S. Weaver, J. J. Brown, and S. R. Forrest, Direct evidence for degradation of polaron excited states in organic light emitting diodes, *J. Appl. Phys.* **105**, 124514 (2009).
- [38] D. Y. Kondakov, J. R. Sandifer, C. W. Tang, and R. H. Young, Nonradiative recombination centers and electrical aging of organic light-emitting diodes: Direct connection between accumulation of trapped charge and luminance loss, *J. Appl. Phys.* **93**, 1108 (2003).

- [39] R. Z. Li, D. K. J. Lin, and Y. Chen, Uniform design: Design, analysis and applications, *Int. J. Mater. Prod. Technol.* **20**, 101 (2004).
- [40] M. A. Baldo, D. F. O'Brien, Y. You, A. Shoustikov, S. Sibley, M. E. Thompson, and S. R. Forrest, Highly efficient phosphorescent emission from organic electroluminescent devices, *Nature (London)* **395**, 151 (1998).
- [41] M. A. Baldo, S. Lamansky, P. E. Burrows, M. E. Thompson, and S. R. Forrest, Very high-efficiency green organic light-emitting devices based on electrophosphorescence, *Appl. Phys. Lett.* **75**, 4 (1999).
- [42] S. Wehrmeister, L. Jaeger, T. Wehlius, A. F. Rausch, T. C. G. Reusch, T. D. Schmidt, and W. Brutting, Combined Electrical and Optical Analysis of the Efficiency Roll-Off in Phosphorescent Organic Light-Emitting Diodes, *Phys. Rev. Applied* **3**, 024008 (2015).
- [43] R. C. Kwong, M. R. Nugent, L. Michalski, T. Ngo, K. Rajan, Y.-J. Tung, M. S. Weaver, T. X. Zhou, M. Hack, M. E. Thompson, S. R. Forrest, and J. J. Brown, High operational stability of electrophosphorescent devices, *Appl. Phys. Lett.* **81**, 162 (2002).
- [44] D. Y. Kondakov, Role of chemical reactions of arylamine hole transport materials in operational degradation of organic light-emitting diodes, *J. Appl. Phys.* **104**, 084520 (2008).
- [45] A. Carbone, B. K. Kotowska, and D. Kotowski, Space-Charge-Limited Current Fluctuations in Organic Semiconductors, *Phys. Rev. Lett.* **95**, 236601 (2005).
- [46] G. Ferrari, D. Natali, M. Sampietro, F. P. Wenzl, U. Scherf, C. Schmitt, R. Guntner, and G. Leising, Current noise spectroscopy on mLPPP based organic light emitting diodes, *Org. Electron.* **3**, 33 (2002).
- [47] Y. Song, H. Jeong, J. Jang, T. Y. Kim, D. Yoo, Y. Kim, and T. Lee, 1/f noise scaling analysis in unipolar-type organic nanocomposite resistive memory, *ACS Nano* **9**, 7697 (2015).
- [48] A. B. Chwang, R. C. Kwong, and J. J. Brown, Graded mixed-layer organic light-emitting devices, *Appl. Phys. Lett.* **80**, 725 (2002).
- [49] Y. Shao and Y. Yang, Naturally formed graded junction for organic light-emitting diodes, *Appl. Phys. Lett.* **83**, 2453 (2003).
- [50] S. W. Liu, X. W. Sun, and H. V. Demir, Graded-host phosphorescent light-emitting diodes with high efficiency and reduced roll-off, *AIP Adv.* **2**, 012192 (2012).
- [51] N. C. Erickson and R. J. Holmes, Engineering efficiency roll-off in organic light-emitting devices, *Adv. Funct. Mater.* **24**, 6074 (2014).
- [52] J. G. Simmons, Potential barrier and emission-limited current flow between closely spaced parallel metal electrodes, *J. Appl. Phys.* **35**, 2472 (1964).